applied sciences

MDPI

Article

Effects of Air Gaps on the Output Force Density in COMSOL Simulations of Biomimetic Artificial Muscles

Michelangelo A. Coltelli and Emil P. Kartalov *

Physics Department, Naval Postgraduate School, Monterey, CA 93943, USA
* Correspondence: epkartal@nps.edu; Tel.: +1-831-656-2125

Featured Application: Improved architectures of artificial muscles for exoskeletal locomotion, undersea drone propulsion, walker vehicles, physical augments, and prosthetics.

Abstract: This paper presents a novel approach to enhancing the performance of artificial muscle fibers by incorporating air gaps within the bulk dielectric material. Building on previous models, the COMSOL simulation was developed to investigate the effects of varying the inner ligament width ('w3') and air gap width ('w2') on force production. Results indicated that an air gap width of 50 μm is optimal, balancing improved force output with manufacturability constraints. A longitudinal array sweep was conducted to determine force density saturation in long fiber arrays, comparing the gap model with a traditional non-gap model. The gap model demonstrated superior performance, achieving higher force densities and better energy efficiency. The inclusion of air gaps reduced overall weight, enhanced flexibility, and improved the force-to-weight ratio, making the design particularly suitable for applications in prosthetics, exoskeletons, and soft robotics. These findings suggest that the air gap design represents a significant advancement in artificial muscle technology, offering a practical and efficient solution for various biomedical and robotic applications.

Keywords: actuator; muscle; fiber; biomimetic; electrostatic; force; simulations; COMSOL; gaps



Citation: Coltelli, M.A.; Kartalov, E.P. Effects of Air Gaps on the Output Force Density in COMSOL Simulations of Biomimetic Artificial Muscles. *Appl. Sci.* **2024**, *14*, 9715. https://doi.org/10.3390/app14219715

Academic Editor: Jihong Yan

Received: 24 July 2024
Revised: 15 October 2024
Accepted: 18 October 2024
Published: 24 October 2024



Copyright: © 2024 by the authors. Licensee MDPI, Basel, Switzerland. This article is an open access article distributed under the terms and conditions of the Creative Commons Attribution (CC BY) license (https://creativecommons.org/licenses/by/4.0/).

1. Introduction

Traditional robotic actuators primarily consist of electric motors and hydraulic systems. Electric step motors [1] are widely used in small robotic systems due to their precision, convenient power usage, and scalability. These motors operate through the Lorentz force, requiring a substantial magnetic field generated by large electric currents through copper solenoids, resulting in significant Joule heating and high-power demands. Electromagnetic motors are most efficient for large displacements but less effective for small displacements [2].

Hydraulic systems represent another major approach and are used in applications such as derricks, cranes, bulldozers, forklifts, industrial robots, and the US Army Mule walking robot [3,4]. However, hydraulic actuators do not scale well with system size, as reducing system size decreases piston area, leading to reduced force at the same pressure. This makes hydraulic systems unsuitable for miniaturization. Additionally, pneumatic actuators produce less force than other solutions at larger displacements [2], and their performance is similar to that of pneumatic artificial muscles [5]. Biomimetic applications, such as exoskeletons and prosthetics, require smooth and precise motion control, which is challenging to achieve with hydraulics [6].

Given these limitations, modern applications like undersea drones, exoskeletal suits, all-terrain walker drones, prosthetics, and medical assist devices are exploring alternative solutions, such as artificial muscles [7,8]. For instance, dielectric elastomer actuators (DEAs) [9–12] utilize the deformation of a polymer slab due to electrostatic forces between charges on electrodes under an external voltage. This force increases inversely with

the square of the distance between electrodes, making it more effective at microscopic scales. Incidentally, the same principle can be used to build a capacitive high-sensitivity gauge of mechanical deformation [13,14], as well as a pressure sensor [15]. DEAs can be arrayed longitudinally to enhance elongation distance and laterally to increase force output. However, the high cost of traditional manufacturing methods limits the scalability of these devices, typically confining them to small applications like single-chamber microrobots [16–18] and HASEL tentacle actuators [19,20]. Although multi-material 3D printing holds promise [21–24], it remains in its early stages.

We have developed an alternative solution [25]: artificial muscles created by 3D printing microfluidic channels, which serve as embedded wires and electrodes for microcapacitors arranged to form muscle fibers [26]. Applying voltage to an array of microcapacitors causes them to contract simultaneously, producing an electrostatic actuation force transmitted via the surrounding polymer material, acting as tendons. These electrostatic actuators are scalable, energy-efficient, and offer a high force-to-weight ratio [25]. COMSOL simulations [25] demonstrated a force density of up to 33 MPa at current fabrication limits, though these simulations were restricted to small devices [25].

The output force density is inversely proportional to the square of the separation distance between the capacitor plates, with optimal results achieved at microscopic scales. The total force of a muscle fiber bundle is the sum of the forces generated by individual fibers arranged in parallel [25,26]. In our previous research, we investigated the scalability of artificial muscle fibers, recognizing that each fiber generates a relatively small force, necessitating tens of thousands of microcapacitors for a practical macro-scale muscle. Direct simulation of such large-scale muscles was computationally prohibitive due to the limitations in computational power. To circumvent this, we hypothesized that the output force density would reach saturation as the array size increased, enabling us to estimate the force of larger arrays without direct simulation.

To test this hypothesis, we used COMSOL to simulate artificial muscle structures at a 100 μm scale, constructed as N × N × 10 arrays of microcapacitors, with N varying from 1 to 13, while also varying tendon thickness within each array. The maximal force density for each configuration was plotted against N, revealing saturation around and beyond N = 10, thus confirming our hypothesis. Consequently, a 10 × 10 × 10 array was found to be representative and predictive of much larger arrays of artificial muscle devices. This result is significant for advancing research and developing practical artificial muscles. The saturation level was approximately 9 kPa at the 100 μm scale, suggesting a force density of about 1 MPa at the 10 μm scale, indicating the feasibility of strong, energy-efficient, low-density muscles for various applications [27].

While force density saturation for the current design was determined, there is still room for optimization of the actuator design. For example, introducing air gaps in the bulk dielectric or ligament of muscle fibers offers several notable advantages. First, air gaps could significantly reduce the overall weight of the artificial muscle, enhancing its force-to-weight ratio and making it more efficient and responsive. This reduction in weight would be beneficial for applications where minimizing mass is crucial, such as in wearable exoskeletons or aerial drones. Additionally, air gaps could improve the flexibility and compliance of the muscle fibers, allowing for more natural and adaptive movements that better mimic biological muscles. This would be essential for applications in prosthetics and soft robotics, where fine motion control and adaptability are required. Moreover, the inclusion of air gaps could increase actuation efficiency, as the reduced material density can lessen the dampening effect the bulk dielectric has on the current electrostatic actuator design. Finally, longitudinal air gaps should allow for the muscle fibers to expand laterally more easily, which should increase the contraction, decrease the plate separation, and thus non-linearly increase the output actuation force.

Herein, we report on the results of COMSOL simulations of air gaps inside the microfluidic artificial muscles. These results show that the air gaps lead to a significant gain in the overall output force density compared to the traditional non-gap architecture. Hence,

this is a theoretical proof of principle for this new approach. This design innovation could thus contribute to the development of stronger, lighter, and more energy-efficient artificial muscles suitable for a wide range of practical applications.

2. Materials and Methods

The development of the COMSOL simulation model builds upon the models of previous papers [25–27]. New Multiphysics features led to updates in the model's development, as described. The basic geometry consists of an overall bulk material in the form of an outer rectangular prism which contains alternating pairs of electrode chambers arranged in parallel within the bulk material. Additionally, channels that span in the z-direction through the entirety of the bulk dielectric are situated between electrode stacks. These cubic channels represent the air gaps. The study employed for this simulation is time-dependent.

2.1. Model Development

The tendon thicknesses 'e' was applied to the bulk dielectric at the device's edge and was set to 50 µm. The space between the plates and the air gaps, 'w3', was nominally 50 µm but was swept to determine its relationship with force output. The top and bottom edge thickness 'c' was kept fixed at 50 µm. The width of the electrode plates in both the x and y directions was defined by 'w1' and set at 400 µm. The electrode plate thickness and spacing in the z-direction 't' was defined as 100 µm. The small width of the air gap, 'w2', was nominally 50 µm but was swept to determine its relationship with force output. The long width of the air gap was the same as the plate width, 'w1'. The parameters are shown below in Figure 1 showing the geometry in side view.

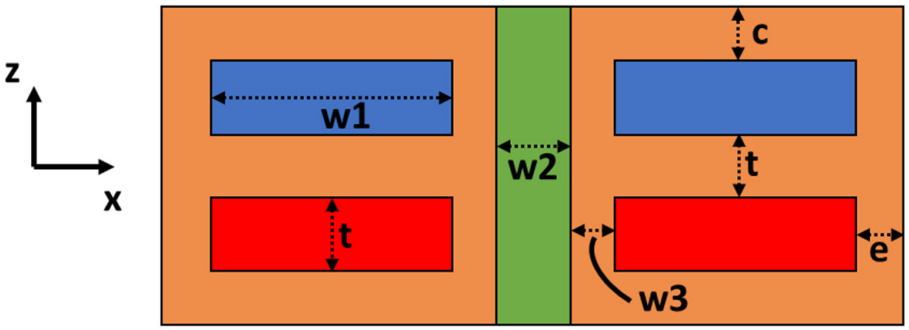


Figure 1. Gap simulation model showing geometric parameters (side view). Electrodes are represented in blue (positive bias) and red (ground). Air gaps are shown in green. The bulk material is shown in orange.

Three physics nodes were utilized: electrostatics, solid mechanics, and laminar flow. The solid mechanics node was applied to the bulk dielectric, the moving mesh node to the electrode chambers along with the air gaps, and the electrostatics node was applied to all domains. To correlate the nodes and affect actuation on the model, the electromechanical forces and fluid–structure-interaction nodes were applied to the model.

To properly define the properties of the model, the following materials from the COMSOL material library were applied to specific areas. PDMS was applied to the bulk dielectric of the actuator (shown in orange in Figure 1), water was applied to the electrode plates (shown in blue and red in Figure 1), and air was applied to the air gaps (shown in green in Figure 1). A potential of 3000 V was applied to all surfaces of one set of electrodes, while a ground potential was applied to the other set. The potential was applied to the model using a ramp function. The ramp function improved convergence significantly during the simulation. This voltage was chosen to ensure that any electrostatically induced deformation would not exceed the dielectric breakdown threshold of PDMS. Figure 2 displays how the electric potential was applied to the model (blue plates represent electrodes with electric potential and red plates represent ground). Dielectric properties were applied to

the different domains using the charge conservation node, which applied properties based on their respective materials.

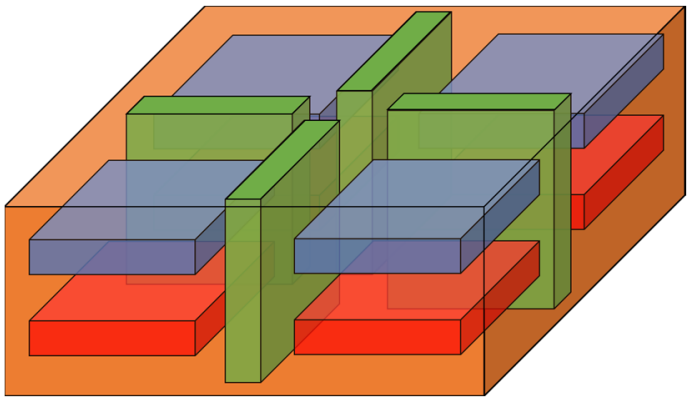


Figure 2. Electrode pattern in the gap simulation model. The blue electrodes on the diagram are biased positively compared to the red electrodes, which are held at ground potential. Air gaps are shown in green. The bulk material is represented in orange.

The mesh developed for the model can be separated into two regions: the bulk dielectric and the air gaps. The model mainly uses a quadratic tetrahedral element excluding the air gaps, which instead use linear tetrahedral elements for computational efficiency for the fluid flow simulations. The bulk dielectric uses a minimum element size of 10 µm. The air gaps use a minimum element size of 3 µm. This smaller minimum mesh size for the air gaps is to ensure appropriate mesh densities for the smaller geometries of the model. The air gaps also featured a layered prism mesh along the faces of the air gaps and pdms boundaries to ensure proper simulation of the no-slip boundary condition. The mesh element dimensions were held constant during parameter-sweep simulations, and the values were determined, due to offering both computational efficiency and accuracy, while optimizing model convergence.

A fixed-boundary node was applied to the top and bottom faces of the bulk dielectric. In a practical application, the muscle would be attached on each end to rigid non-slip plates interfacing with the outside world. That condition is fairly represented by the boundaries chosen herein. The material was defined as linear elastic for the purpose of this simulation. Figure 3 displays the solid mechanics boundary conditions in black hashes on the top and bottom face of the model. These boundary conditions are analogous to applying a tensile load on a cantilever beam. The simulation calculates the stress generated at this boundary condition to determine the load applied.

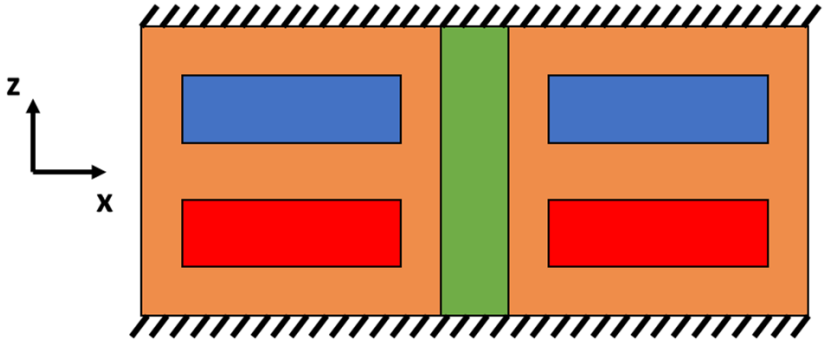


Figure 3. Gap model displaying the displacement boundary conditions.

To allow for deformation of the non-solid domains of the model, the deforming domain node was applied to both the water electrodes and the air gaps. The laminar flow node was applied to the air gaps. The open boundary node was applied to the faces of the air gaps coincident with the top and bottom faces of the bulk dielectric (the faces perpendicular to the z-axis). The wall node was applied to the remaining faces of the air gaps with the no-slip condition. The electromechanical forces module allows for the strain of the bulk dielectric based on the electrostatic forces between the electrodes. The fluid–structure-interaction Multiphysics node couples the interaction of the air gap domain and the solid dielectric. The objective of this feature is to determine the impact of deforming fluid gaps on the actuation of the artificial muscle fiber. The force density of the fiber array was determined by integrating the stress tensor in the z-direction (solid.szz) over the top surface of the fiber array. This value was then divided by the total area of the top surface of the model (including the top of the air gaps) to determine the effective force density.

2.2. Description of Analysis

The analysis involved the use of a COMSOL model to investigate the impact of air gaps within the bulk dielectric or ligament of artificial muscle fibers. This study focused on varying the air gap width ('w2'), with the goal to determine the effect on force production. We separately investigated the force density saturation of longitudinal fiber arrays and the impact that air gaps have vs. the traditional design.

2.2.1. Varying Air Gap Width

Air gap width ('w2') was varied independently with all other parameters held nominally to assess its effect on force production. By running a parametric sweep varying 'w2' from 20 μm to 200 μm using a step size 10 μm, we aimed to quantify how the introduction of and variation in air gaps influenced the electrostatic forces generated within the muscle fibers. The force output was measured and compared to the non-gap design, providing insights into the efficacy of this new design. These values were compared to the non-gap model, where 'w2' was zero.

2.2.2. Longitudinal Array Sweep of the Gap Model

A longitudinal array sweep was conducted to determine the force density saturation in long fiber arrays. This involved modeling arrays of muscle fibers with varying lengths and configurations to assess how the force density scaled with array size. The parameter scaled was 'n2', which represents the number of microcapacitors (or electrode pairs) in the vertical direction. The analysis included a detailed examination of force density saturation points, which indicate the maximum effective force production achievable before additional length no longer contributes to increased force output.

2.2.3. Longitudinal Array Sweep of the Non-Gap Model

To evaluate the effectiveness of the air gap design, a longitudinal array sweep was also performed on a non-gap model. This comparison involved using the same parameters as the air gap model except for 'w2' being zero. The force densities from both models were compared to determine the advantages or disadvantages of incorporating air gaps. Figure 4 shows the $2 \times 2 \times 1$ gap model with nominal dimensions. The plot shows the stress in the bulk dielectric along with the flow velocity in the air gaps at peak actuation (t = 2 s). The air gaps are clearly deforming, which displays the influence of fluid–structure interaction on the model. This influence is further highlighted by the clear display of fluid movement in the air gaps. The low fluid speeds can be attributed to the high resistance of the narrow microfluidic channels and the model being initially at an equilibrated state of pressure.

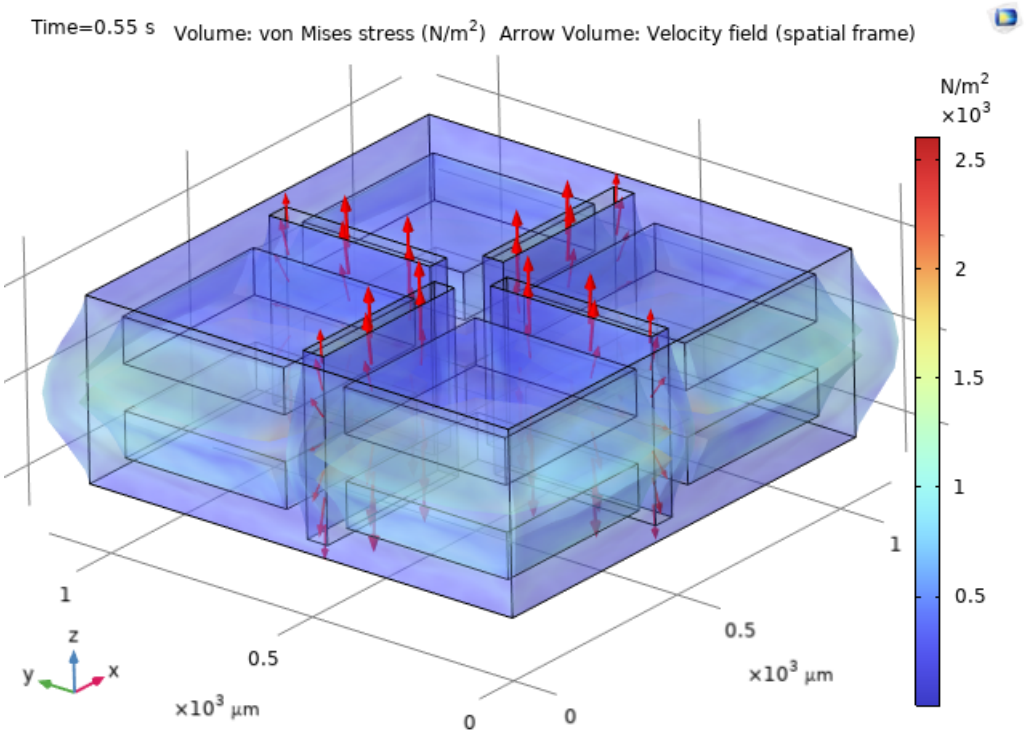


Figure 4. 2 × 2 × 1 air gap simulation plot showing stress in the bulk dielectric and fluid velocity in the air gaps.

3. Results

The analysis of varying the air gap width ('w2') within the bulk dielectric produced the data plotted in Figure 5. They indicate a significant impact on the force production of the artificial muscle fibers. As 'w2' was adjusted, the force output exhibited a peak at lower gap widths. Specifically, the force production was found to be optimal at 'w2' values around 50 µm. While smaller gap widths continued to increase force density, practical manufacturing constraints make these smaller dimensions less feasible. Therefore, 50 µm has been selected as the ideal parameter for 'w2', balancing enhanced force production with manufacturability.

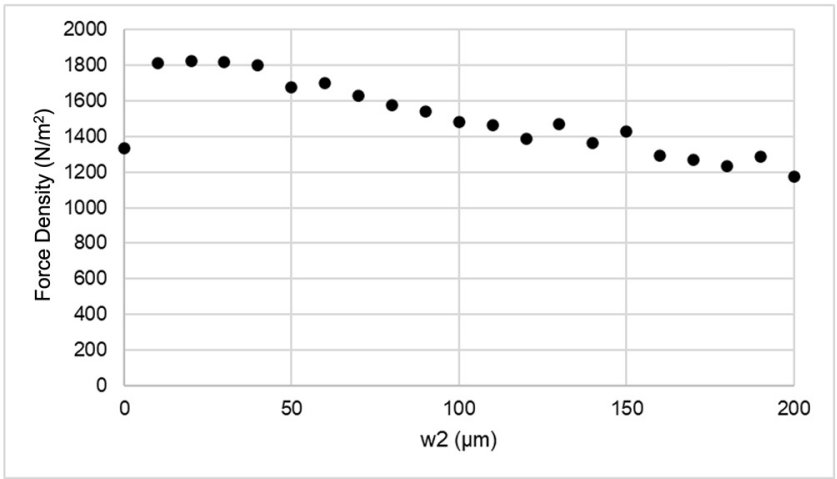


Figure 5. Parameter sweep of gap width 'w2' vs. force density for a 2 × 2 × 1 gap model.

To determine the force density saturation of long fiber arrays, a longitudinal array sweep was conducted. Arrays of varying lengths and configurations were modeled to assess how the force density scales with the size of the array. During the length sweep, the gap width was set to a constant 50 µm, due to the considerations explained above. The simulation results are shown in Figure 6. They indicate a trend toward force density saturation as the number of microcapacitors in the array increase. This saturation point indicates the maximum effective force production achievable before additional length no longer contributes significantly to increased force output. Comparison revealed that the gap model outperformed the non-gap model in terms of force density, demonstrating the advantages of the air gap design in enhancing actuator efficiency.

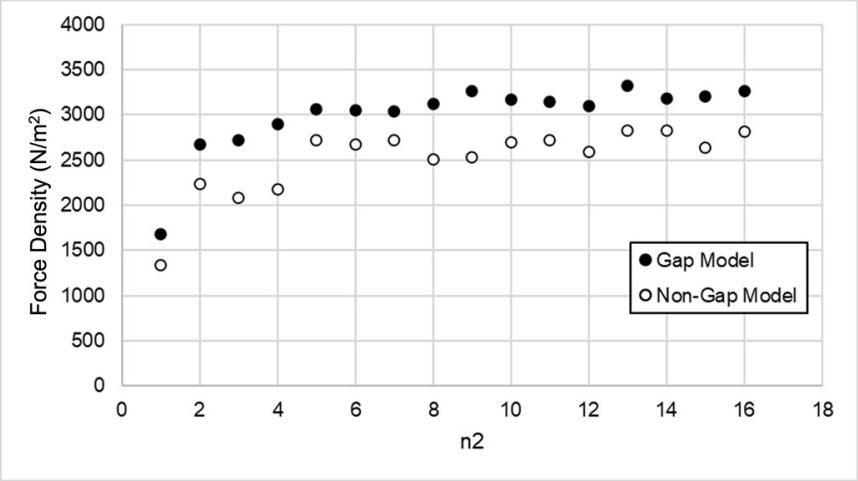


Figure 6. Longitudinal array sweep of 'n2' (number of devices) for gap models with a 50 µm gap width (black circles) and non-gap models (empty circles).

The simulated numerical results in Figure 4 were validated by comparing them with the results of the previous simulations and first principle back-of-the envelope calculations [25].

4. Discussion

The results of this study highlight several key advancements in the design and performance of artificial muscle fibers with the incorporation of air gaps. The optimization of the air gap width ('w2') at 50 µm demonstrates a significant improvement in force production compared to traditional designs without air gaps. This enhancement is achieved by balancing manufacturability and performance, ensuring that the selected gap width is practical for real-world applications. Comparative analysis with the non-gap model further underscores the advantages of the gap model.

In this study, we have introduced a transient modeling approach to enhance the accuracy and physical validity of simulations compared to the static model used in previous works. The static simulations described in previous communications were limited by their assumption of a constant force application on a non-deformed geometry, which does not capture the dynamic interactions between forces and deformations observed in real-world conditions. Our transient model, however, accounts for the time-dependent evolution of forces and their effects on the device geometry, incorporating a feedback loop that updates forces based on the changing geometry. In particular, this approach is crucial for gapped devices, where geometry significantly influences force distribution and the performance of the fluid–structure-interaction Multiphysics module. Future work should use this simulation approach to produce more realistic results, especially for higher-resolution representative designs of the physical prototype.

The force density saturation observed in the longitudinal array sweep indicates that both model types achieve higher force densities as 'n2' increases. The gap model outperforms the non-gap model for all values of 'n2'. The air gap design also improves energy efficiency by reducing material density, thereby lowering the capacitance and power consumption needed for actuation. While saturation is not achieved in this study due to computational limitations, the air gap design does improve actuation efficiency.

The increase in force density due to the gap technique would be useful to any application that can benefit from a high ratio of force to mass, such as exoskeletal locomotion, powered armor, physical augments and prosthetics, and unmanned underwater vehicles (UUVs), which require low-profile actuation with high force production [28].

These theoretical results must also be viewed in the context of current cutting-edge 3D printing techniques. Recent developments [29–32] in 3D-printed embedded microfluidics (achieved by using Stratasys PolyJet printers in conjunction with new clearance techniques of sacrificial material) have shown reliable fabrication and successful clearing of embedded microfluidic channels down to a 400 μm width and, in some cases, down to a 200 μm width. When these results are compared with our own theoretical results presented herein, the apparent conclusion is that PolyJet-printed devices are only a step or two away from reaching gap widths that would make the gap technique worthwhile in enhancing force density output. Separately, new SLA printers are poised to achieve features at the scale of tens of microns. Even if negative features and embedded channels would require resolution tradeoffs, it is clear that the gap technique described herein would either already or soon will be quite useful in practical applications.

5. Conclusions

The introduction of air gaps within artificial muscle fibers represents a significant improvement over the traditional design. The optimized air gap width of 50 μm balances manufacturability with enhanced performance, making it a viable solution for various practical applications. Further research and development could explore the additional optimization of these parameters and the application of this design to other types of actuators, potentially expanding the range of effective and efficient artificial muscle technologies. With a minimal increase to the cross-sectional area of the fiber, the open-gap design offers significant force increases that can lower the cross-sectional area of a fiber bundle at a given operation force.

Author Contributions: Conceptualization, M.A.C. and E.P.K.; methodology, M.A.C.; software, M.A.C.; validation, M.A.C.; formal analysis, M.A.C. and E.P.K.; investigation, M.A.C. and E.P.K.; resources, E.P.K.; data curation, M.A.C.; writing—original draft preparation, M.A.C.; writing—review and editing, M.A.C. and E.P.K.; visualization, M.A.C. and E.P.K.; supervision, E.P.K.; project administration, E.P.K.; funding acquisition, E.P.K. All authors have read and agreed to the published version of the manuscript.

Funding: This research was funded by the Office of Naval Research, grant numbers N0001422WX01543 and N0001423WX01092.

Institutional Review Board Statement: Not applicable.

Informed Consent Statement: Not applicable.

Data Availability Statement: Data available upon reasonable request.

Acknowledgments: The authors thank the Office of Naval Research for providing the funding for the work. The authors thank Jeffrey Catterlin from NPS for assembling and debugging the super desktop computer used for the simulations.

Conflicts of Interest: The authors declare no conflicts of interest.

References

1. Liptak, B. *Instrument Engineers' Handbook*, 4th ed.; CRC Press: Boca Raton, FL, USA, 2003.
2. Tavakoli, M.; Marques, L.; de Almeida, A. A comparison study on pneumatic muscles and electrical motors. In Proceedings of the 2008 IEEE International Conference on Robotics and Biomimetics, Bangkok, Thailand, 22–25 February 2009.
3. Richardson, A.; Rodgers, M. Vison-Based Semi-Autonomous Outdoor Robot System to Reduce Soldier Workload. In *Proceedings of SPIE 4364, Unmanned Ground Vehicle Technology III*; SPIE: Bellingham, WA, USA, 2001; Volume 4364, pp. 12–18.
4. Ali, H.I.; Noor, S.B.; Marhaban, M.H.; Bashi, S.M. Design of H-inf Controller with Tuning of Weights Using Particle Swarm Optimization. *IAENG Int. J. Comput. Sci.* **2011**, *38*, 103–112.
5. Tiwari, R.; Meller, M.A.; Wajcs, K.B.; Moses, C.; Reveles, I.; Garcia, E. Hydraulic artificial muscles. *J. Intell. Mater. Syst. Struct.* **2012**, *23*, 301–312. [CrossRef]
6. Zoss, A.; Kazerooni, H. Design of an electrically actuated lower extremity exoskeleton. *Adv. Robot.* **2006**, *20*, 967–988. [CrossRef]
7. Mirvakili, S.M.; Hunter, I.W. Artificial Muscles: Mechanism, applications, and challenges. *Adv. Mater.* **2018**, *30*, 1704407. [CrossRef]
8. Zhang, J.; Sheng, J.; O'Neill, C.T.; Walsh, C.J.; Wood, R.J.; Ryu, J.H.; Desai, J.P.; Yip, M.C. Robotic Artificial Muscles: Current Progress and Future Perspectives. *IEEE Trans. Robot.* **2019**, *35*, 761–781. [CrossRef]
9. Bahramzadeh, Y.; Shahinpoor, M. A Review of Ionic Polymeric Soft Actuators and Sensors. *Soft Robot.* **2014**, *1*, 38–52. [CrossRef]
10. Feng, C.; Rajapaksha, C.H.; Jákli, A. Ionic Elastomers for Electric Actuators and Sensors. *Engineering* **2021**, *7*, 581–602. [CrossRef]
11. Akle, B.J.; Bennett, M.D.; Leo, D.J. High-strain ionomeric–ionic liquid electroactive actuators. *Sens. Actuators A Phys.* **2006**, *126*, 173–181. [CrossRef]
12. Duduta, M.; Hajiesmaili, E.; Zhao, H.; Wood, R.J.; Clarke, D.R. Realizing the potential of dielectric elastomer artificial muscles. *Proc. Natl. Acad. Sci. USA* **2019**, *116*, 2476–2481. [CrossRef]
13. Zhang, H.; Wang, M.Y. Multi-Axis Soft Sensors Based on Dielectric Elastomer. *Soft Robot.* **2016**, *3*, 3–12. [CrossRef]
14. Wang, H.; Totaro, M.; Beccai, L. Toward Perceptive Soft Robots: Progress and Challenges. *Adv. Sci.* **2018**, *5*, 1800541. [CrossRef]
15. Lei, K.F.; Lee, K.-F.; Lee, M.Y. Development of a flexible PDMS capacitive pressure sensor for plantar pressure measurement. *Microelectron. Eng.* **2012**, *99*, 1–5. [CrossRef]
16. Christians, C.; Goldberg, N.N.; Deheyn, D.D.; Cai, S.; Tolley, M.T. Translucent soft Robots driven by frameless fluid electrode dielectric elastomer actuators. *Sci. Robot.* **2018**, *3*, eaat1893. [CrossRef] [PubMed]
17. Pelrine, R.E.; Kornbluh, R.D.; Joseph, J.P. Electrostriction of polymer dielectrics with compliant electrodes as a means of actuation. *Sens. Actuators A Phys.* **1998**, *64*, 77–85. [CrossRef]
18. Shi, Y.; Askounis, E.; Plamthottam, R.; Libby, T.; Peng, Z.; Youssef, K.; Pu, J.; Pelrine, R.; Pei, Q. A processable, high-performance dielectric elastomer and multilayering process. *Science* **2022**, *377*, 228–232. [CrossRef]
19. O'Neill, M.R.; Acome, E.; Bakarich, S.; Mitchell, S.K.; Timko, J.; Keplinger, C.; Shepherd, R.F. Rapid 3D Printing of Electrohydraulic (HASEL) Tentacle Actuators. *Adv. Funct. Mater.* **2020**, *30*, 2005244. [CrossRef]
20. Martinez, R.V.; Branch, J.L.; Fish, C.R.; Jin, L.; Shepherd, R.F.; Nunes, R.M.; Suo, Z.; Whitesides, G. Robotic Tentacles with Three-Dimensional Mobility Based on Flexible Elastomers. *Adv. Mater.* **2013**, *25*, 205–212. [CrossRef]
21. Chortos, A.; Mao, J.; Mueller, J.; Hajiesmaili, E.; Lewis, J.A.; Clarke, D.R. Printing Reconfigurable Bundles of Dielectric Elastomer Fibers. *Adv. Funct. Mater.* **2021**, *31*, 2010643. [CrossRef]
22. Shaukat, U.; Rossegger, E.; Schlögl, S. A Review of Multi-Material 3D Printing of Functional Materials via Vat Photopolymerization. *Polymers* **2022**, *14*, 2449. [CrossRef]
23. Knowlton, S.; Yu, C.H.; Ersoy, F.; Emadi, S.; Khademhosseini, A.; Tasoglu, S. 3D-printed microfluidic chips with patterned, cell-laden hydrogel constructs. *Biofabrication* **2016**, *8*, 025019. [CrossRef]
24. Rafiee, M.; Farahani, R.D.; Theriault, D. Multi-Material 3D and 4D Printing: A Survey. *Adv. Sci.* **2020**, *7*, 1902307. [CrossRef] [PubMed]
25. Coltelli, M.A.; Catterlin, J.; Scherer, A.; Kartalov, E.P. Simulations of 3D-printable biomimetic artificial muscles based on microfluidic microcapacitors for exoskeletal actuation and stealthy underwater propulsion. *Sens. Actuators A Phys.* **2021**, *325*, 112700. [CrossRef]
26. Coltelli, M.A.; Kartalov, E.P. Scalable microfluidic double-helix weave architecture for wiring of microscopic arrays in 3D-printable biomimetic artificial muscles. *Sens. Actuators A Phys.* **2022**, *340*, 113543. [CrossRef]
27. Coltelli, M.; Keeven, J.; Catterlin, J.; Sadagic, A.; Kartalov, E. Output Force Density Saturation in COMSOL Simulations of Biomimetic Artificial Muscles. *Appl. Sci.* **2023**, *13*, 9286. [CrossRef]
28. Kerrebrock, P.A.; Anderson, J.M.; Parry, J.R. Application requirements of artificial muscles for swimming robots. In *Smart Structures and Materials 2001: Electroactive Polymer Actuators and Devices*; SPIE: Bellingham, WA, USA, 2001; Volume 4329, pp. 364–374.
29. Hornik, T.; Terry, M.; Krause, M.; Catterlin, J.K.; Joiner, K.L.; Aragon, S.; Sarmiento, A.; Arias-Thode, Y.M.; Kartalov, E.P. Experimental Proof of Principle of 3D-Printed Microfluidic Benthic Microbial Fuel Cells (MBMFCs) with Inbuilt Biocompatible Carbon-Fiber Electrodes. *Micromachines* **2024**, *15*, 870. [CrossRef] [PubMed]
30. Krause, M.; Marshall, A.; Catterlin, J.K.; Hornik, T.; Kartalov, E.P. Dimensional fidelity and orientation effects of PolyJet technology in 3D printing of negative features for microfluidic applications. *Micromachines* **2024**, *15*, 389. [CrossRef]

31. Hornik, T.; Kempa, J.; Catterlin, J.; Kartalov, E. A qualitative experimental proof of principle of self-assembly in 3D printed microchannels towards embedded wiring in biofuel cells. *Micromachines* **2023**, *14*, 807. [CrossRef]
32. Hornik, T.; Kempa, J.; Catterlin, J.; Kartalov, E. A solution to the clearance problem of sacrificial material in 3D printing of microfluidic devices. *Micromachines* **2022**, *14*, 16. [CrossRef]

Disclaimer/Publisher's Note: The statements, opinions and data contained in all publications are solely those of the individual author(s) and contributor(s) and not of MDPI and/or the editor(s). MDPI and/or the editor(s) disclaim responsibility for any injury to people or property resulting from any ideas, methods, instructions or products referred to in the content.